Nano Research 2016, 9(5): 1366–1376
DOI 10.1007/s12274-016-1032-y
Research Article

ISSN 1998-0124
CN 11-5974/O4

Monodisperse hollow silica spheres: An in-depth scattering analysis

Pia Ruckdeschel[1], Martin Dulle[2], Tobias Honold[3], Stephan Förster[2], Matthias Karg[3], and Markus Retsch[1] (✉)

[1] *Physical Chemistry 1 – Polymer Systems, University of Bayreuth, Universitätsstr. 30, 95447 Bayreuth, Germany*
[2] *Physical Chemistry 1, University of Bayreuth, Universitätsstr. 30, 95447 Bayreuth, Germany*
[3] *Physical Chemistry 1 – Colloidal Systems, University of Bayreuth, Universitätsstr. 30, 95447 Bayreuth, Germany*

Received: 16 December 2015
Accepted: 25 January 2016

© Tsinghua University Press and Springer-Verlag Berlin Heidelberg 2016

KEYWORDS

hollow sphere,
silica nanoparticle,
small angle X-ray scattering,
light scattering,
nanoscale characterization

ABSTRACT

Herein, we fabricate hollow silica nanoparticles with exceptionally narrow size distributions that inherently possess two distinct length scales—tens of nanometers with regards to the shell thickness, and hundreds of nanometers in regards to the total diameter. We characterize these structures using dynamic and static light scattering (DLS and SLS), small angle X-ray scattering (SAXS), and transmission electron microscopy (TEM), and we demonstrate quantitative agreement among all methods. The ratio between the radius of gyration (SLS) and hydrodynamic radius (DLS) in these particles equals almost unity, corresponding to ideal capsule behavior. We are able to resolve up to 20 diffraction orders of the hollow sphere form factor in SAXS, indicating a narrow size distribution. Data from light and X-ray scattering can be combined to a master curve covering a q-range of four orders of magnitude assessing all hierarchical length scales of the form factor. The measured SLS intensity profiles noticeably change when the scattering contrast between the interior and exterior is altered, whereas the SAXS intensity profiles do not show any significant change. Tight control of the aforementioned length scales in one simple and robust colloidal building block renders these particles suitable as future calibration standards.

1 Introduction

The ability to generate highly defined, hierarchically structured materials from a few nanometers in size to several micrometers is a key prerequisite for the realization of future functional devices. Potential applications for such structured materials lie in the fields of energy conversion, energy storage, catalysis, and separation [1–4]. Two strategies are currently used to obtain such structures, namely top-down and bottom-up approaches. Top-down approaches allow for exquisite control of the symmetry and shape of the desired nanostructure. Bottom-up approaches rely on the self-assembly of molecular or colloidal building blocks into superstructures of defined length scales and symmetries [5, 6]. Their size and shape translate

Address correspondence to markus.retsch@uni-bayreuth.de

directly into the assembled superstructure [7, 8]. Quite expectedly, any short-comings such as ill-defined shapes or a wide distribution in particle size can deteriorate the properties of bottom-up constructed devices and structures.

For building blocks which range from a few nm up to several μm in size, scattering techniques such as small angle X-ray scattering (SAXS) or light scattering (dynamic: DLS or static: SLS) are well-established and commonly being used. These techniques, which yield reciprocal space information, can be complemented by imaging techniques such as atomic force microscopy (AFM), and scanning or transmission electron microscopy (SEM or TEM) [9, 10]. On the contrary, all of these techniques require reliable standards for instrument calibration. In particular for scattering techniques, current calibration standards such as Ag-behenate [11–13], Ag-stearate [13], or rat collagen [14, 15] only embody one single length scale and are susceptible to light degradation or dehydration. Alternatively, narrowly distributed colloidal suspensions consisting of polystyrene, poly(methylmethacrylate), or silica are being used [16–20]. In these cases, several standards of different sizes must be employed to cover the desired q-range. This can be overcome by using monodisperse silica hollow spheres.

Such hollow sphere structures have increasingly been in the focus of academic research [10, 21]. Their potential applications in areas such as dye-sensitized solar cells, gas sensors, heterogeneous catalysis, super capacitors, or drug delivery vehicles [10, 21] capitalize on the high surface area, microporosity and free volume of these materials. Furthermore, due to their intrinsically hierarchical structure (the overall particle diameter and the shell thickness), hollow spheres are a powerful platform for generating three-dimensional materials that embody multiple length scales.

In this communication, we employ hollow silica nanoparticles with an extremely small polydispersity. This allows us to resolve unprecedented details in ensemble averaging techniques, which are typically compromised by the particle size distribution. In particular, we compare the characterization by TEM, DLS, SLS, and SAXS. We discuss in detail how these methods can be used to extract in-depth information and emphasize the potential application of silica capsules as a calibration standard material. Furthermore, we investigate the influence of the scattering contrast within such particles on these different scattering techniques.

2 Results and discussion

We focus on three distinct hollow sphere types, which are based on the same template core particle but with increasing shell thickness. These are denoted "A-500", "B-500", and "C-500" with increasing shell thickness, respectively. The number indicates the temperature of calcination, either 500 or 950 °C. TEM imaging is able to resolve overall structural information (particle diameter and shell thickness) as well as local information on the homogeneity of the capsule. Figure 1 shows a two-dimensional projection of the hollow spheres, deposited on a carbon coated grid.

The shell thickness can be determined from the dark rim around the hollow center, which represents the area of highest matter density along the electron beam path. Since we used the same template particles for all variants, the outer diameter accordingly increases with increasing shell thickness. The particles cover a range

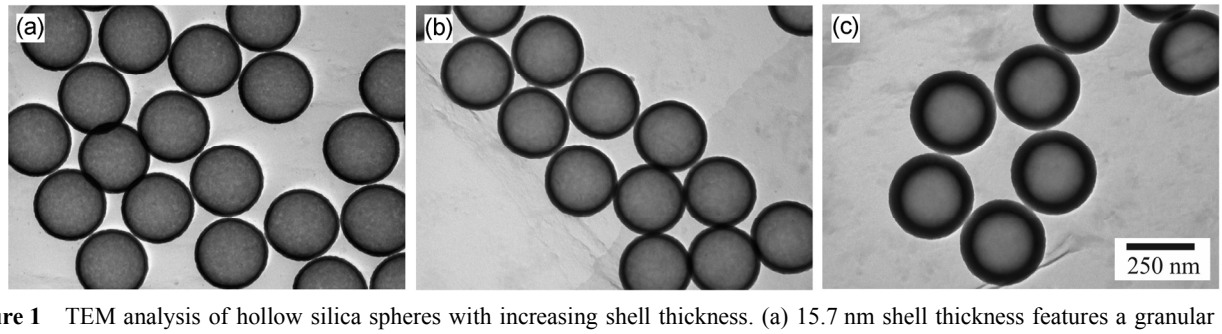

Figure 1 TEM analysis of hollow silica spheres with increasing shell thickness. (a) 15.7 nm shell thickness features a granular shell, which becomes smoother with increasing silica layer thickness to (b) 21.4 nm and (c) 43.7 nm.

from 131 to 158 nm in radius. The shell thicknesses were measured to be 15.7 nm (A-500), 21.4 nm (B-500), and 43.7 nm (C-500). TEM gives additional qualitative insight into the homogeneity of the shell, as can be deduced from the gray scale contrast across the hollow center. One can recognize that a slight variation on a length scale of a few nanometers is visible for the thinnest shell, which can be explained by the fabrication process. During Stöber condensation, silicate nanoclusters nucleate in the ethanolic dispersion and precipitate onto the oppositely charged template surface. Further growth of these initial clusters leads to the formation of a homogenous surface, which becomes smoother as the shell thickness increases. It is also apparent that the polystyrene (PS) core removal step by calcination does not impact the integrity of the silica shell, nor does it change the crystallinity (see X-ray diffraction (XRD) spectra of amorphous silica material in Fig. S1 in the Electronic Supplementary Material (ESM)). The integrity of the silica shell can also be confirmed by the SEM images shown in Fig. S2 and Fig. S3(a) in the ESM. No holes or cracks are visible. Furthermore, the particles can be redispersed on an individual level with no clustering or sintered necks evident in the TEM images.

To study the sizes and size distributions of the hollow particles on a statistical ensemble, we employed both dynamic and static light scattering techniques. Figure 2(a) shows typical intensity-time autocorrelation functions measured at a scattering angle of 45°, which is sufficiently lower than the first form factor minimum of the colloids. All correlation functions show a monomodal decay, which could be analyzed using inverse Laplace transformation based on the CONTIN algorithm (red solid lines). The distribution functions of the hydrodynamic radius R_h obtained from this CONTIN analysis (Fig. 2(b)) provide only single size distributions with small variances. In order to prove the diffusive behavior of the particles in these dispersions, angle dependent measurements were performed. The mean relaxation rates Γ obtained from CONTIN analysis of each autocorrelation function depend linearly on the square of the scattering vector q and feature intercepts close to zero (Fig. 2(c)). This is indicative of purely translational diffusion being probed in the scattering volume.

However, the inset in Fig. 2(c) shows a slight dependence of the apparent diffusion coefficient $D_{T,\mathrm{app}} = \frac{\Gamma}{q^2}$ on the scattering angle. One possible explanation for this angle dependence is a concentration effect within the hollow sphere dispersion. In order to determine the hydrodynamic radius with very high accuracy, we extracted the translational diffusion coefficient by linear regression of the angular dependent data shown in the inset in Fig. 2(c). The intercept of the linear fits provide the diffusion coefficients $D_{T,0}$ according to $D_{T,\mathrm{app}} = D_{T,0}(1 + A \cdot q^2)$. The respective hydrodynamic radii R_h obtained from the diffusion coefficients using the Stokes–Einstein equation $\left(D_{T,0} = \frac{k_B T}{6\pi\eta R_h}\right)$ are listed in Table 1. The

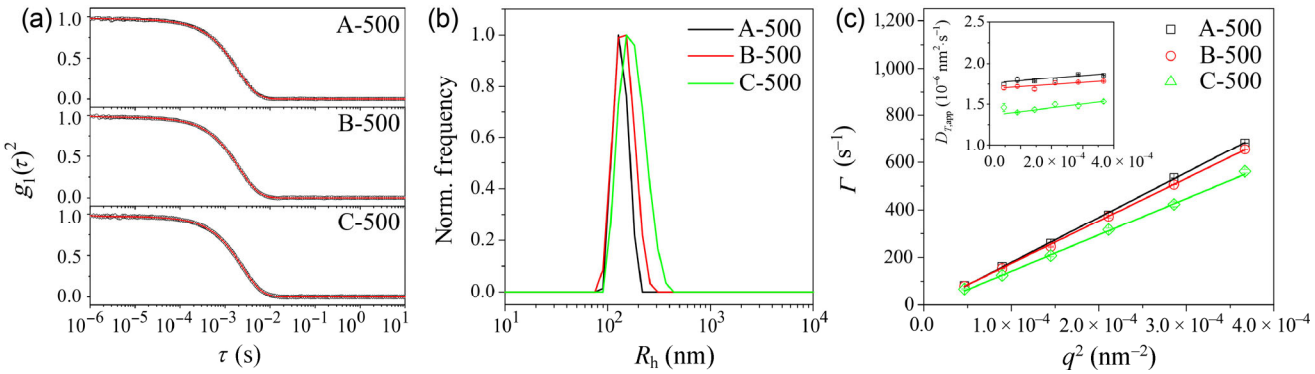

Figure 2 DLS analysis of hollow spheres after redispersion in water. (a) Intensity–time autocorrelation functions recorded at a scattering angle of 45°. The red solid lines are fits from CONTIN analysis. (b) Distribution of the hydrodynamic radius as obtained from the relaxation rate distributions G(Γ) from CONTIN analysis of the autocorrelation data. (c) Angle-dependent analysis of the relaxation rate Γ. The inset demonstrates a slight dependency of the diffusion coefficient on the scattering angle.

Table 1 Summary of the results from DLS and SLS measurements at 25 °C

Sample	DLS	SLS	R_g/R_h	SLS			TEM	
	R_h (nm)	R_g[a] (nm)		R_{hollow}[b] (nm)	$R_{C/S}$[c] (nm)	ΔR[c] (nm)	R (nm)	d_{shell} (nm)
A-500	138 ± 3	136 ± 1	0.988	126	133	14.6	131 ± 2	15.7 ± 1.0
B-500	144 ± 2	142 ± 1	0.987	129	140	21.6	135 ± 2	21.4 ± 0.8
C-500	179 ± 1	166 ± 1	0.928	143	167	48.6	158 ± 1	43.7 ± 1.6

[a]The values were obtained from the slope analysis of linear fits in the Guinier plots shown in Fig. 3 (first 8 data points were not considered). Considering all data points measured with the HeNe laser (632.8 nm) the values are 134, 139, and 165 nm for sample A-500, B-500, and C-500.

[b]These values were obtained from fits to the SLS scattering curves using a form factor model for an ideal hollow sphere with infinitely thin shell using Eq. (1).

[c]These values were obtained from fits to the SLS scattering curves using a form factor model for a spherical core/shell particle using Eqs. (2) and (3).

hydrodynamic radii increase from sample A-500 to C-500 with increasing shell thickness, which agrees with the results from TEM analysis.

SLS was used to investigate the radius of gyration R_g and the form factor $P(q)$ of the samples. Due to the relatively small size of the particles, the Guinier region is sufficiently covered for measurements at small angles. Figure 3(a) shows the results of SLS measurements in the low q limit in a Guinier representation. All datasets show a linear dependence and could be analyzed by linear regression (solid lines) providing the radius of gyration according to $\ln(I) = -\frac{q^2 R_g^2}{3}$. The obtained values for R_g are listed in Table 1, and increase as the shell thickness increases (A-500 to C-500). For an ideal homogeneous hollow sphere with an infinitely thin shell, the ratio between R_g and R_h should equal unity. By contrast, for a solid sphere one would expect a ratio of R_g/R_h = 0.775. In fact, sample A-500, which has the thinnest silica shell, has a ratio R_g/R_h = 0.988 which is very close to unity. As expected, this ratio decreases with increasing shell thickness.

Figure 3(b) shows the scattering intensity as a function of the scattering vector as obtained from SLS. In order to cover a broad range of momentum transfer values q, we employed two lasers with different wavelength (632.8 and 532 nm) for the SLS investigation and merged the datasets by simple multiplication with constant multipliers. The first form factor minimum is resolved for all samples in the higher q region of

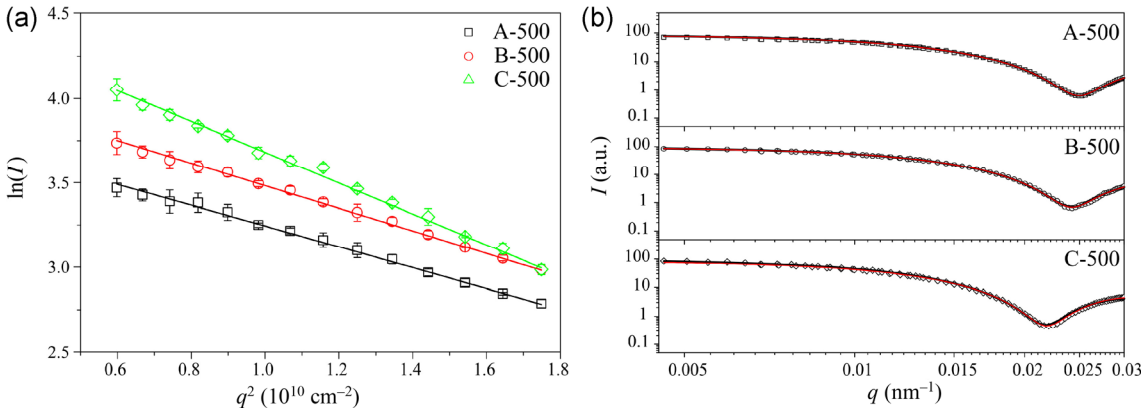

Figure 3 Results from SLS measurements: (a) Guinier plot for hollow spheres with increasing shell thickness. The solid lines are linear fits. (b) Form factor analysis demonstrates a minimum at high q, which shifts to lower q for larger particle diameters, i.e., particles with increasing shell thickness. The red solid lines are fits using a form factor of hollow spheres with an infinitely thin wall according to Eq. (1). The black solid lines are fits using a form factor for spherical core–shell particles according to Eqs. (2) and (3). The scattering contrast of the core was set equal to the surrounding medium (water).

the SLS profiles. As the shell thickness increases, the position of the minimum shifts to lower q values, which is in good agreement with the increasing particle radii. As a first attempt to describe the experimental data, we used the simple form factor model for hollow spheres with infinitely thin shells to fit the SLS data, as shown in Eq. (1)

$$I\left(q, R_{\text{hollow}}\right) = \left(\frac{\sin qR_{\text{hollow}}}{qR_{\text{hollow}}}\right)^2 \tag{1}$$

The fits using this model are shown as red lines in Fig. 3(b). Very good agreement between the experimental data and this fit is found for all samples. The sphere radii from this analysis are listed in Table 1 and follow the radii trend determined from DLS and TEM. Compared to the values of R_g from Guinier analysis, the sphere radii from this simple form factor (Eq. (1)) are slightly smaller, which illustrates that the shell thickness is finite.

Due to the high quality and the small error bars of the SLS data, we elected to employ a more complex form factor model to describe the experimental data. For this we used the spherical core–shell model presented in Eqs. (2) and (3) [22]

$$\begin{aligned} &I(q, R, \Delta R, \Delta\eta_1, \Delta\eta_2) = \\ &[K(q, R+\Delta R, \Delta\eta_2) - K(q, R, \Delta\eta_2 - \Delta\eta_1)]^2 \end{aligned} \tag{2}$$

with

$$K\left(q, R, \Delta\eta\right) = \frac{4}{3}\pi R^3 \Delta\eta \cdot 3 \cdot \frac{\sin qR - qR\cos qR}{(qR)^3} \tag{3}$$

Here, R is the radius of the core, ΔR the thickness of the shell, $\Delta\eta_1$ the scattering contrast between the core and the surrounding matrix (in this case $\Delta\eta_1 = 0$, implying that the core of the hollow spheres is infiltrated by water) and $\Delta\eta_2$ the scattering contrast between the shell and the matrix (water). The radius of the core–shell particle is consequently $R_{\text{C/S}} = R + \Delta R$. The fits are shown as black lines in the graphs of Fig. 3(b). Again the fits describe the experimental data very accurately. The values for R and ΔR obtained from this analysis are listed in Table 1. The values for the shell thickness are very close to the values obtained from TEM analysis, and show the expected increase in shell thickness from sample A-500 to C-500. The sphere radii show the same tendency and are in very good agreement with the radii obtained from TEM. Moreover, the radii from this form factor analysis are very close to the values of R_g obtained from Guinier analysis.

The results from DLS and SLS measurements reveal the very low polydispersity in size and shell thickness of all three hollow particle systems. They perform as well as known colloidal particle standards, but have the advantage of assessing a second length scale—the shell thickness—in SLS measurements. Furthermore, looking at the R_g/R_h ratio, hollow silica spheres can be considered as calibration standards for both DLS and SLS.

However, these light scattering measurements are restricted to very low values of q and the form factor is only partially accessible. Hence, we used SAXS (Fig. 4) covering a much broader q-range and in particular larger values of q to investigate the form factor and size distribution of the colloids. The high contrast of the silica hollow spheres (in air) makes it possible to measure to very low q values of 0.026 nm^{-1} in our SAXS setup (see Experimental Part 4.4) and it also results in a very good signal/noise ratio even at high q values. The samples were measured as dry powder in air. The first apparent feature in all SAXS measurements is the low polydispersity of the different spheres. Usually the form factor minima that arise from the overall size of such a hollow sphere are smeared out due to slight size variations. In contrast, all our samples under investigation show many form factor oscillations (over two orders of magnitude in q). In the case of these samples, the usually negligible effect of pinhole smearing is the main reason for the suppression of highest orders of form factor oscillations.

It is apparent that the scattering profile comprises two sorts of contributions: one originating from the total particle size, one from the shell thickness. The particle radius results in narrowly spaced oscillating modes, for which up to 20 diffraction orders can be resolved. These are superimposed by fewer oscillations originating from the silica shell. While only one minimum can be inferred for the 15 nm shell, up to six additional minima contribute to the scattering profile in case of the 44 nm shell. The SAXS curves were quantitatively analyzed by the same core–shell

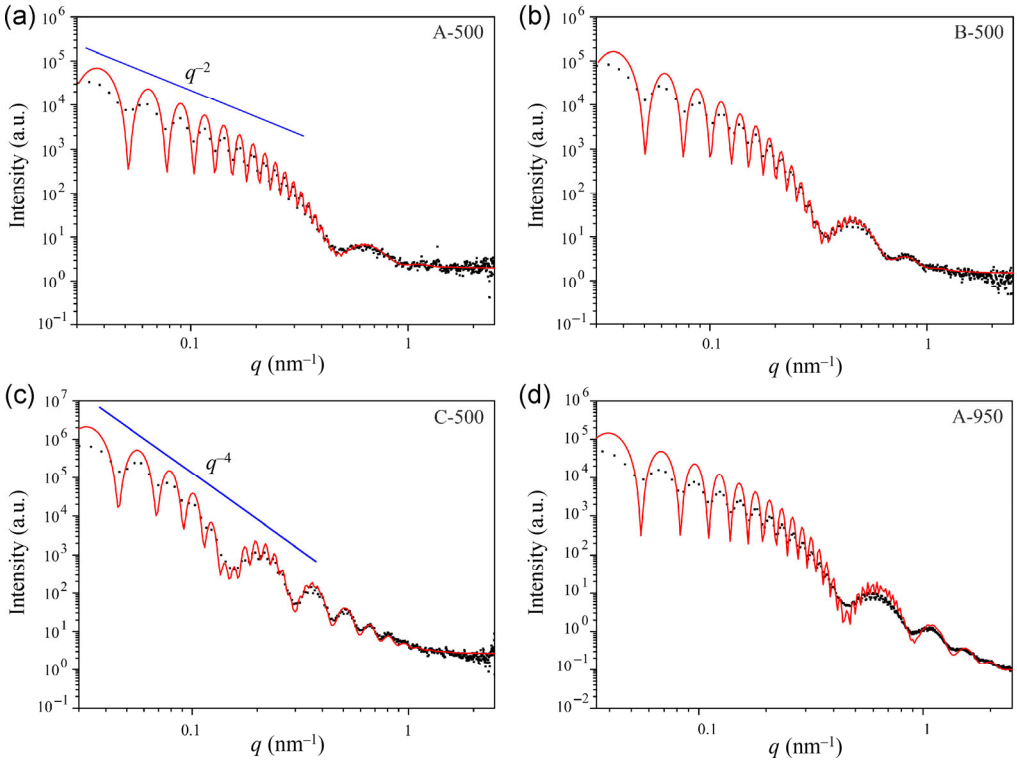

Figure 4 SAXS analysis of hollow silica spheres (black dots) and the corresponding fits using a form factor for spherical core–shell particles (red lines). (a)–(c) Due to the monodispersity of the hollow sphere particles, up to 20 diffraction orders can be resolved. The scattering profile consists of the superposition of contributions from the total particle diameter and the shell thickness, respectively. The shell thickness increases from 14 nm (A-500), to 19 nm (B-500), and 43 nm (C-500). The initial slope decreases from q^{-2} to q^{-4} indicating a change in local curvature. (d) Calcination of sample A at 950 ˚C leads to microstructural changes within the SiO_2 network, which result in an even better resolved SAXS spectrum.

model as the SLS data. The fits to the data are the red lines in Fig. 4. The model can very accurately describe the scattering of the different samples and allows us to obtain very precise values for the shell thickness and total particle radius. The fitted data are summarized in Table 2. The agreements for both the shell thickness and total particle radius are excellent compared to TEM and SLS. For comparison, the TEM data are listed in Table 2 as well.

When the shell thickness increases, the local environment around a hollow sphere changes. Its scattering properties transition towards the behavior of solid spheres, which can also be seen in the SAXS curves. The initial decay of intensity with momentum transfer shifts from q^{-2} (sample A-500) to q^{-4} (sample C-500). This is due to the local curvature that is very small in the case of sample A-500, similar to a thin flat sheet. When the shell thickness is increased, this changes and starts to resemble the curvature of a solid sphere.

Another interesting effect can be observed by calcination of sample A at high temperatures (950 ˚C). As discussed recently, calcination at elevated temperatures leads to a range of microstructural changes within a SiO_2 network [23]. These changes are reflected in an even better resolved SAXS curve, especially in the high q-region. The background is reduced by one order of magnitude and allows for an even more precise evaluation of size and polydispersity (see Table 2). As mentioned previously, all samples are so narrowly distributed that the pin hole setup with a beam size of 100 μm × 100 μm and a 300 K Pilatus detector is causing more smearing than the sample itself. We interpret this sharpening of the SAXS spectrum as a decrease of randomly distributed scattering sites within the silica shell, which manifests itself in a decrease of Brunauer–Emmett–Teller (BET) surface area and a loss in microporous volume [23]. The overall geometry of

Table 2 Summary of the results from SAXS measurements and comparison to TEM analysis

Sample	SAXS					TEM	
	R_o (nm)	σ (R_o)	R_i (nm)	σ (R_i)	d_{shell} (nm)	R (nm)	d_{shell} (nm)
A-500	128.0	0.15	114.5	0.015	13.5	131 ± 2	15.7 ± 1.0
B-500	134.0	0.09	115.0	0.015	19.0	135 ± 2	21.4 ± 0.8
C-500	157.5	0.04	115.0	0.020	42.5	158 ± 1	43.7 ± 1.6
A-950	120.5	0.06	106.5	0.011	14.0	123 ± 2	15.9 ± 1.1

the hollow sphere remains unchanged during the calcination process. The form factor fitting yields an outer and inner radius R_o = 120.5 nm and R_i = 106.5 nm, respectively, which corresponds to a shrinkage of about 6%. The shell thickness remains unchanged at d_{shell} = 14.0 nm. For comparison the TEM images of the sample A-950 are shown in the Figs. S3(b) and S3(c) in the ESM. Size and shell thickness data are listed in Table 2 as well. The TEM measurements are comparable to the SAXS data, showing a shrinkage of 6%.

Hollow silica spheres feature a range of advantages over existing calibration standards. They possess a high scattering contrast (SiO_2–air), which reduces the measurement time necessary to obtain low-noise spectra, and embody two length scales in their form factor, which can be precisely tuned from 10 nm to several hundreds of nm. Furthermore, SiO_2 is a chemically robust material, which is stable as an aqueous colloidal dispersion as well as dry powder and does not need to be protected from light or heat. The colloidal stability is underpinned by the light scattering data of sample B-500*, measured more than six months after redispersion in water (see Fig. S4 and Table S1 in the ESM). The form factor analysis demonstrates no detectable changes to the monodispersity or the particle dimensions.

In order to fully assess the hierarchical structure of hollow silica spheres, we demonstrate the possibility to combine the form factor data from SLS and SAXS into a single master curve (Fig. 5(a)). As can be seen, the respective q-ranges hardly overlap, but can be nicely stitched together to result in a full q-range coverage of almost four orders of magnitude. With appropriate adjustment of the absolute scattering intensity, this master curve can be built for all three samples under investigation. This full master curve can then be fitted again by the core–shell form factor (Eq. (2)), as shown in Fig. 5(b). The fit curve (red line) captures all relevant features of both the SLS and SAXS data.

This master curve is only accessible when comparable relative scattering contrasts are present in both the

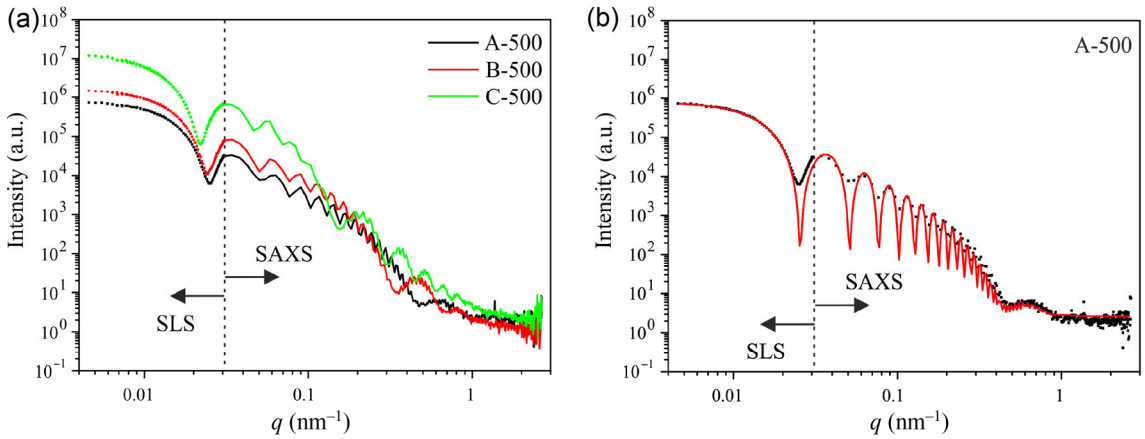

Figure 5 Superposition of SLS and SAXS data. (a) Adjusting the absolute scattering intensities of SLS and SAXS measurements allows for the construction of a master curve. The scattering data span a range of almost four orders of magnitude for the samples under investigation. (b) All structural features of the master curve can be fitted by a single analysis using a core–shell form factor.

SLS and SAXS measurements. We demonstrate this through the investigation of air-filled (empty) silica spheres dispersed in water. Such particles are accessible via calcination at 950 ˚C, which closes the micropores in the silica shell as demonstrated previously [23]. For the case of the thickest shell (sample C-950), the micropores are completely closed so that water does not enter, as shown in the cryo TEM images in Figs. S5(b) and S5(c) in the ESM.

The SLS measurements of sample C-950 (see Fig. 6(a)) show that different scattering contrasts between the core and the surrounding matrix strongly influences the SLS profile ($\Delta\eta_1$ from Eq. (2) changes from $\Delta\eta_1 = 0$ to $\Delta\eta_1 < 0$). Instead of a minimum at high q values, a broad maximum is present for sample C-950. The dashed red line represents a simulation of the form factor using the same geometric parameters, but with an adjusted scattering contrast to resemble the air-filled core. By contrast, SAXS is not sensitive to this change in scattering contrast, as the scattering cross section of the Si atoms in the shell is the dominant contribution in this case. This is corroborated by the nearly identical SAXS profiles of the dry powder (indicated by vertical grey lines in Fig. 6(b)) and its water-filled and dispersed counterpart (C-500). Consequently, the shape of the form factor is not altered. A slight shift towards higher q values in the case of C-950 can be explained by a small shrinkage during calcination, analogous to sample A-950 outlined above (see Table S2 in the ESM).

We find a similar trend for sample B-950 with a thinner shell. In this case, however, some capsules can still be infiltrated by water leading to a mixture of empty and water filled silica capsules (see Fig. S5(a) in the ESM). The SLS profile therefore presents an intermediate between the fully filled and fully empty case (Fig. S6 in the ESM).

3 Conclusions

In this report, we demonstrated a detailed and thorough analysis of hollow silica particles with impressively narrow size distributions. These hierarchically structured objects comprise two distinct length scales: the total particle radius (hundreds of nm) and the shell thickness (tens of nm). We used TEM, (angle-dependent) DLS, SLS, and SAXS measurements to fully describe their structural features and scattering properties. The size of the hollow spheres ranged from 131 to 158 nm in radius and 16 to 44 nm in shell thickness, respectively. Our results show an outstanding quantitative consistency among the various methods. These hollow spheres possess a close to ideal capsule morphology with the ratio R_g/R_h approaching 1 for the thinnest, yet stable, shell. We further investigated the scattering properties of these hollow spheres over a range of four

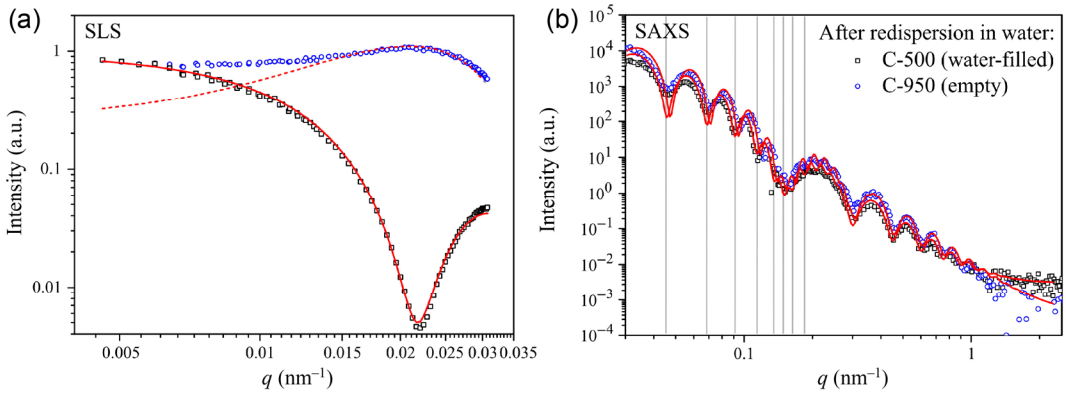

Figure 6 Influence of the scattering contrast. (a) Form factor analysis by static light scattering. SLS data of water-filled C-500 (black squares) and air-filled C-950 (blue circles) in water. The red line is the corresponding fit of sample C-500 using a form factor for spherical core–shell particles with equal scattering contrasts of the core and the surrounding medium (see Fig. 3(b)). The red dotted line is a simulation of the form factor for spherical core–shell particles with different scattering contrasts between the core (air) and the surrounding medium (water). All data shown are normalized to 1. (b) SAXS analysis of hollow silica spheres C-500 (black squares) and C-950 (blue circles) after redispersion in water. The SAXS curves were quantitatively analyzed by the same core–shell model as the SLS data. The small shift of the form factor towards higher q-values is due to a small amount of shrinkage of the hollow spheres upon calcination at 950 ˚C.

orders of magnitude. A simple core–shell form factor analysis is sufficient to describe all structural features across all length scales. SAXS analysis gave further insight into the bending curvature, which transitions from membrane-like towards solid spheres as the shell thickness increases. Changes to the relative scattering contrast between the particle interior and exterior led to marked changes in the SLS data, whereas the intensity profile of the SAXS measurement was not influenced by these changes.

This detailed analysis can be used as reference and guidance for the investigation of well-defined colloidal objects. While the presented methods are being considered "standard" techniques and have been widely applied in many fields, we want to emphasize the good agreement between ideal theoretical models and the corresponding experimental data. Furthermore, we advocate monodisperse hollow silica spheres to be used as a calibration standard for small angle scattering experiments in the future. Their core advantages are their high scattering contrast for visible light and X-rays, long-term stability as dry powders and aqueous dispersions, and their incorporation of two defined length scales.

4 Experimental

4.1 Materials

Styrene (⩾99%, Aldrich), 2,2′-azobis(2-methylpropionamidine) dihydro- chloride (AIBA; 97%, Aldrich), 2-methacryloxy-ethyltrimethylammonium chloride (MTC; 70% solution in water, Polyscience), polyvinylpyrrolidone K30 (PVP; M_W ~ 55 kg·mol^{-1}, Aldrich), tetraethyl orthosilicate (TEOS; ⩾99%, Aldrich) and ammonium hydroxide solution (30%–33% in water, Aldrich) were purchased and used as received. Ethanol (EtOH) was used in technical grade and water was taken from a Millipore Direct Q3UV unit for all synthesis and purification steps.

4.2 Synthesis of monodisperse hollow silica nanoparticles

The synthesis of monodisperse hollow silica nanoparticles is a three-step process. First, monodisperse PS latex particles were synthesized by emulsifier-free emulsion polymerization, carried out in a 500 mL three-neck flask equipped with a gas inlet and a reflux condenser. Solid chemicals were dissolved in water prior to addition. To start, 200 mL water, 26 mL styrene, 1.8 g PVP, and 100 μL MTC were heated to 70 °C at a stirring speed of 850 rpm using a large egg-shaped magnetic stirring bar. After equilibrating for 20 min, 600 mg AIBA initiator, dissolved in 40 mL water, was quickly added to initiate the polymerization. After nucleation, the stirring speed was reduced to 450 rpm and the polymerization was allowed to continue overnight at 70 °C under a slight inert gas flow. In the second step, the PS template particles were coated with silica shells to obtain core/shell particles using a Stöber condensation process [24]. Various amounts of TEOS were added to an 81.2 vol.% EtOH, 10.7 vol.% H_2O, 6.1 vol.% NH_4OH solution containing 10.7 g·L^{-1} PS latex beads. Thin, medium, and thick shells were achieved by adjusting the TEOS content to 2.1 vol.%, 3.2 vol.%, and 8.7 vol.%, respectively. The condensation reaction was conducted at room temperature overnight at a stirring speed of 500 rpm with a magnetic stirring bar. The core/shell particles were purified by repeated centrifugation and redispersion in water. In order to prepare hollow spheres, samples were dried and calcined in a furnace (Nabertherm L5/11/P33) at 500 °C or 950 °C in air for 12 h. These hollow spheres could be redispersed in water using mild sonication in a sonication bath.

4.3 Light scattering measurements

SLS and DLS measurements were performed on a standard goniometer setup (ALV, Langen, Germany) equipped with a HeNe laser (JDSU, USA) with λ = 632.8 nm and a maximum output power of 35 mW, as well as a Verdi V-2 (Coherent, USA) with λ = 532 nm and a maximum output power of 2 W. All measurements were performed at 25 °C. The temperature was adjusted using a toluene matching/temperature bath. The temperature was controlled by a PT100 thermocouple placed in the bath next to the sample. For SLS measurements, angular steps of 2° were performed in a range of 25°–155° (λ = 532 nm) and 20°–60° (λ = 632.8 nm) to cover a q-range of 0.005–0.03 nm^{-1}. DLS measurements were performed in an angular range of 25°–75° (λ = 532 nm) in steps of 10°. Three intensity-time autocorrelation functions were recorded at each

step. The samples were prepared from dry material. A small amount of the solid was dispersed in water using 30 min of sonication at low power (50%). When the sample was completely dispersed, a small amount of the dispersion was further diluted with water and filtered using a 5 μm PTFE syringe filter. The sample was directly filtered into dust-free cylindrical quartz cells for light scattering. The intensity-time auto-correlation functions measured in DLS were analyzed using an inverse Laplace transformation with the CONTIN algorithm using the software After ALV 1.0d by Dullware. This analysis provided the average relaxation rate $<\Gamma>$ as a function of scattering angle. The SLS data measured using two different laser wavelengths were merged and fitted using the SASfit software (version 0.93.2) by J. Kohlbrecher [22].

4.4 SAXS measurements

All SAXS data reported here were measured using the small angle X-ray system "Double Ganesha AIR" (SAXSLAB, Denmark). The X-ray source in this system was a rotating anode (copper, MicoMax 007HF, Rigaku Corporation, Japan) providing a micro-focused beam at λ = 0.154 nm. Data were recorded by a position sensitive detector (PILATUS 300K, Dectris). Different detector positions were used to cover the range of scattering vectors between 0.026–2.5 nm^{-1}. The samples were put inside a small envelope made of kapton (powder) or filled in a capillary (liquid samples). The circularly averaged data were normalized to the incident beam, the sample thickness and the measurement time before subtraction of the signal of the kapton envelope/air. The resulting curves from the different detector distances were then merged to yield one curve. The fitting was performed using Scatter with the vesicle model [25].

4.5 TEM measurements

TEM images were collected on a Zeiss CEM 902 instrument in bright field imaging mode at an acceleration voltage of 80 kV. Samples were prepared by dropping 10 μL of a diluted colloidal dispersion of redispersed silica hollow nanoparticles onto carbon coated copper grids. After 10 s, the excess solution was blotted with filter paper.

For cryo TEM imaging, diluted colloidal dispersions of redispersed silica hollow spheres were dropped on copper grids coated with a lacey carbon film. Subsequently, most of the liquid was blotted with filter paper, leaving a thin film stretched over the holes. The samples were then instantly shock frozen by plunging them rapidly into liquid ethane and cooled to approximately 90 K by liquid nitrogen in a temperature-controlled freezing unit (Zeiss Cryobox). The frozen specimen was inserted into a cryo transfer holder (CT3500, Gatan) and transferred to a Zeiss EM922 Omega energy-filtered TEM instrument. Imaging was carried out at an acceleration voltage of 200 kV and temperatures around 90 K.

4.6 XRD measurements

Powder XRD measurements were carried out using a STOE STADI P (CuKα1 radiation) diffractometer in transmission geometry, equipped with a fast, high resolution silicon strip detector DECTRIS Mythen1K. The samples were mounted on a flat disk using Scotch® tape. A step size of 0.2° and integration time of 20 s were used.

Acknowledgements

The German Research Foundation (No. SFB840) funded this project. P. R. thanks the Elite Network Bavaria (ENB) and the University of Bayreuth Graduate School. We acknowledge Dr. Markus Drechsler for assistance with the cryo TEM measurements, Tobias Kemnitzer for XRD measurements, and Dr. Sabine Rosenfeldt for fruitful discussions.

Electronic Supplementary Material: Supplementary material (further TEM and SEM images, cryo TEM images, and XRD data) is available in the online version of this article at http: //dx.doi.org/10.1007/s12274-016-1032-y.

References

[1] Choi, H.; Sofranko, A. C.; Dionysiou, D. D. Nanocrystalline TiO_2 photocatalytic membranes with a hierarchical mesoporous multilayer structure: Synthesis, characterization, and multifunction. *Adv. Funct. Mater.* **2006**, *16*, 1067–1074.

[2] Rhee do, K.; Jung, B.; Kim, Y. H.; Yeo, S. J.; Choi, S. J.; Rauf, A.; Han, S.; Yi, G. R.; Lee, D.; Yoo, P. J. Particle-nested inverse opal structures as hierarchically structured large-scale membranes with tunable separation properties. *ACS Appl. Mater. Interfaces* **2014**, *6*, 9950–9954.

[3] Su, B.-L.; Sanchez, C.; Yang, X.-Y. *Hierarchically Structured Porous Materials: From Nanoscience to Catalysis, Separation, Optics, Energy, and Life Science*; Wiley-VCH Verlag GmbH & Co. KGaA: Weinheim, 2011.

[4] Cho, C.-Y.; Moon, J. H. Hierarchical twin-scale inverse opal TiO_2 electrodes for dye-sensitized solar cells. *Langmuir* **2012**, *28*, 9372–9377.

[5] Wang, D. Y.; Möhwald, H. Template-directed colloidal self-assembly–the route to 'top-down' nanochemical engineering. *J. Mater. Chem.* **2004**, *14*, 459–468.

[6] von Freymann, G.; Kitaev, V.; Lotsch, B. V.; Ozin, G. A. Bottom-up assembly of photonic crystals. *Chem. Soc. Rev.* **2013**, *42*, 2528–2554.

[7] Vogel, N.; Retsch, M.; Fustin, C. A.; Del Campo, A.; Jonas, U. Advances in colloidal assembly: The design of structure and hierarchy in two and three dimensions. *Chem. Rev.* **2015**, *115*, 6265–6311.

[8] Gröschel, A. H.; Walther, A.; Löbling, T. I.; Schacher, F. H.; Schmalz, H.; Müller, A. H. E. Guided hierarchical co-assembly of soft patchy nanoparticles. *Nature* **2013**, *503*, 247–251.

[9] Cosgrove, T. *Colloid Science: Principles, Methods and Applications*, 2nd ed.; Wiley-Blackwell: Oxford, 2010.

[10] Chen, Z. H.; Kim, C.; Zeng, X. B.; Hwang, S. H.; Jang, J.; Ungar, G. Characterizing size and porosity of hollow nanoparticles: SAXS, SANS, TEM, DLS, and adsorption isotherms compared. *Langmuir* **2012**, *28*, 15350–15361.

[11] Blanton, T. N.; Huang, T. C.; Toraya, H.; Hubbard, C. R.; Robie, S. B.; Louër, D.; Göbel, H. E.; Will, G.; Gilles, R.; Raftery, T. JCPDS—International Centre for Diffraction Data round robin study of silver behenate. A possible low-angle X-ray diffraction calibration standard. *Powder Diffr.* **1995**, *10*, 91–95.

[12] Huang, T. C.; Toraya, H.; Blanton, T. N.; Wu, Y. X-ray powder diffraction analysis of silver behenate, a possible low-angle diffraction standard. *J. Appl. Crystallogr.* **1993**, *26*, 180–184.

[13] Nyam-Osor, M.; Soloviov, D. V.; Yu, S. K.; Zhigunov, A.; Rogachev, A. V.; Ivankov, O. I.; Erhan, R. V.; Kuklin, A. I. Silver behenate and silver stearate powders for calibration of SAS instruments. *J. Phys.: Conf. Ser.* **2012**, *351*, 012024.

[14] Orgel, J. P. R. O.; Irving, T. C.; Miller, A.; Wess, T. J. Microfibrillar structure of type I collagen *in situ*. *Proc. Natl. Acad. Sci. USA* **2006**, *103*, 9001–9005.

[15] Orgel, J. P. R. O.; Miller, A.; Irving, T. C.; Fischetti, R. F.; Hammersley, A. P.; Wess, T. J. The *in situ* supermolecular structure of type I collagen. *Structure* **2001**, *9*, 1061–1069.

[16] Patel, I. S.; Schmidt, P. W. Small-angle X-ray scattering determination of the electron density of the particles in a colloidal suspension. *J. Appl. Crystallogr.* **1971**, *4*, 50–55.

[17] Russell, T. P. An absolute intensity standard for small-angle X-ray scattering measured with position-sensitive detectors. *J. Appl. Crystallogr.* **1983**, *16*, 473–478.

[18] Perret, R.; Ruland, W. Glassy carbon as standard for the normalization of small-angle scattering intensities. *J. Appl. Crystallogr.* **1972**, *5*, 116–119.

[19] Russell, T. P.; Lin, J. S.; Spooner, S.; Wignall, G. D. Intercalibration of small-angle X-ray and neutron scattering data. *J. Appl. Crystallogr.* **1988**, *21*, 629–638.

[20] Dreiss, C. A.; Jack, K. S.; Parker, A. P. On the absolute calibration of bench-top small-angle X-ray scattering instruments: A comparison of different standard methods. *J. Appl. Crystallogr.* **2006**, *39*, 32–38.

[21] Chen, M.; Ye, C. Y.; Zhou, S. X.; Wu, L. M. Recent advances in applications and performance of inorganic hollow spheres in devices. *Adv. Mater.* **2013**, *25*, 5343–5351.

[22] Kohlbrecher, J. *SASfit: A Program for Fitting Simple Structural Models to Small Angle Scattering Data.* Paul Scherrer Institute, Laboratory for Neutron Scattering: Villigen, Switzerland, 2014.

[23] Ruckdeschel, P.; Kemnitzer, T. W.; Nutz, F. A.; Senker, J.; Retsch, M. Hollow silica sphere colloidal crystals: Insights into calcination dependent thermal transport. *Nanoscale* **2015**, *7*, 10059–10070.

[24] Stöber, W.; Fink, A.; Bohn, E. Controlled growth of monodisperse silica spheres in the micron size range. *J. Colloid Interface Sci.* **1968**, *26*, 62–69.

[25] Förster, S.; Apostol, L.; Bras, W. Scatter: Software for the analysis of nano- and mesoscale small-angle scattering. *J. Appl. Crystallogr.* **2010**, *43*, 639–646.